Ergodicity and Earthquake Catalogs: Forecast Testing and Resulting Implications

K. F. Tiampo,[1] W. Klein,[2] H.-C. Li,[3] A. Mignan,[4] Y. Toya,[1] S. Z. L. Kohen-Kadosh,[1] J. B. Rundle,[5] and C.-C. Chen[3]

Abstract—Recently the equilibrium property of ergodicity was identified in an earthquake fault system (Tiampo *et al.*, Phys. Rev. Lett. *91*, 238501, 2003; Phys. Rev. E *75*, 066107, 2007). Ergodicity in this context not only requires that the system is stationary for these networks at the applicable spatial and temporal scales, but also implies that they are in a state of metastable equilibrium, one in which the ensemble averages can be substituted for temporal averages when studying their behavior in space and time. In this work we show that this property can be used to identify those regions of parameter space which are stationary when applied to the seismicity of two naturally-occurring earthquake fault networks. We apply this measure to one particular seismicity-based forecasting tool, the Pattern Informatics index (Tiampo *et al.*, Europhys. Lett. *60*, 481–487, 2002; Rundle *et al.*, Proc. National Acad. Sci., U.S.A., Suppl. 1, *99*, 2463, 2002), in order to test the hypothesis that the identification of ergodic regions can be used to improve and optimize forecasts that rely on historic seismicity catalogs. We also apply the same measure to synthetic catalogs in order to better understand the physical process that affects this accuracy. We show that, in particular, ergodic regions defined by magnitude and time period provide more reliable forecasts of future events in both natural and synthetic catalogs, and that these improvements can be directly related to specific features or properties of the catalogs that impact the behavior of their spatial and temporal statistics.

Key words: Earthquake forecasting, ergodic behavior, PI method, Thirumalai–Mountain metric, Canadian seismicity, Taiwanese seismicity.

[1] Department of Earth Sciences, University of Western Ontario, London, ON N6A 5B7, Canada. E-mail: ktiampo@uwo.ca

[2] Department of Physics, Boston University, Boston, MA 02215, USA.

[3] Institute of Geophysics, National Central University, Jhongli 320, Taiwan, ROC.

[4] Risk Management Solutions, Science and Technology Research, London, UK.

[5] Center for Computational Science and Engineering, University of California, Davis, CA 95616, USA.

1. Introduction

In recent years, several different forecasting methods based upon the quantification of patterns in seismicity data but relying on different approaches, have been proposed with varying degrees of success (Mogi, 1969; Ogata, 1992; Bufe and Varnes, 1993; Dodge *et al.*, 1996; Bowman *et al.*, 1998; Keilis-Borok, 1999; Orihara *et al.*, 2002; Tiampo *et al.*, 2002; Evison and Rhoades, 2004; Holliday *et al.*, 2007; Papazachos *et al.*, 2007; Mignan, 2008b). This approach tends to result in forecasting techniques which either are related to an inferred or hypothesized underlying physical process, or are purely statistical in nature. The behavior and origin of the precursory seismicity patterns determined by this approach therefore often remain obscure and difficult to comprehend. This lack of understanding presents a significant barrier to understanding the accuracy of these methods, the best route to improving their forecasting capability, and the possible limits to their accuracy as imposed by the physics of the process.

Over the past several years we have pursued the idea that at least some earthquake fault systems behave in the same way as a thermal system in equilibrium; or more precisely in punctuated equilibrium. Integral to this theory is the hypothesis that small to moderate earthquakes can be treated as fluctuations of a system in thermal equilibrium but large events represent a different class. Large events drive the system out of equilibrium, which after some time is re-established until the next large event again forces the system out of equilibrium. This scenario was developed from the study of

models of earthquake faults (FERGUSON et al., 1999; KLEIN et al., 1997) although the picture of punctuated equilibrium was recently verified in some real fault systems (TIAMPO et al., 2003, 2007). In this work, it was demonstrated that the application of a measure of ergodicity commonly used in materials science, the Thirumalai–Mountain (TM) fluctuation metric (THIRUMALAI et al., 1989), could be used to define the ergodic ranges of the seismic catalog, during which the statistics of the natural catalogs were stationary. The intriguing aspect of this discovery is that the property of punctuated equilibrium appears to be associated with the effectiveness of the Pattern Informatics (PI) method for forecasting large events (TIAMPO et al., 2002; HOLLIDAY et al., 2006a; TOYA et al., 2009). Specifically, those fault systems that display punctuated equilibrium, in which periods of ergodic behavior define equilibrium behavior, have large ($M \geq 5$) events that are forecast by the PI method with considerable accuracy, while the accuracy of the PI method on systems that do not display punctuated equilibrium is severely diminished.

The supposition that we wish to test here is that the accurate forecasting of large events using techniques based on isolating fluctuations in the seismicity rate, either quiescence or activation, are dependent on an accurate assessment of the spatial and temporal averages. Although the impact on the stationary behavior of these averages may vary depending on the particular technique and the significance of those averages to a particular technique, the PI method is particularly relevant for this study. As will be shown in Section 2.2, the calculation of the PI index includes both the mean and variance of the regional, or background, seismicity in its functional form and therefore is particularly sensitive to the behavior of these quantities.

Here we present results from two different tectonic regions, eastern Canada and Taiwan, and synthetic catalogs. These analyses provide evidence that the statistics of natural fault systems are ergodic over particular spatial and temporal scales. This property is used to define the extent and nature of specific parameter ranges and spatial and temporal regions in which long-term spatial and temporal averages are both stationary and equivalent. We then employ the PI index to test the hypothesis that earthquake forecasting methodologies based upon linearized analyses of seismic catalog data require that certain equilibrium properties, such as stationarity, are necessary to produce accurate, effective results, and that ergodicity measures can be used to quantify the spatial and temporal scales for which the fault network behaves as an equilibrium system in order to improve these forecasts.

This paper is organized as follows: In Section 2 we present the two methodologies employed in this study, the TM metric and the PI index. In Section 3 we present analysis and results for two select tectonic regions, eastern Canada and Taiwan. In the last subsection of Section 3 we introduce the development and analysis of synthetic catalogs. In Section 4 we summarize our results and conclusions.

2. Method

2.1. Thirumalai–Mountain Metric

The TM fluctuation metric, as originally proposed by Thirumalai and Mountain, measures effective ergodicity, or the difference between the time average of a quantity, generally related to the energy, E_i, at each site, and its ensemble average over the entire system (THIRUMALAI et al., 1989; MOUNTAIN and THIRUMALAI, 1992; THIRUMALAI and MOUNTAIN, 1993). A necessary condition for ergodicity is stationarity, so that regions of phase space identified as effectively ergodic are maintaining stationary statistics over a given period of time. During those time periods, the temporal and spatial averages are equal, and can be substituted for one another. In addition, it is a behavior generally limited to equilibrium states. A system in equilibrium is said to have statistical symmetry, meaning that it is impossible to distinguish individual particles in terms of the averaged properties associated with those particles (THIRUMALAI and MOUNTAIN, 1993). Practically, if the actual measurement time is finite, but long enough, most of the accessible phase space of a system will be equally likely sampled, and the system is effectively ergodic.

E_i is a given quantity which characterizes the energy, or a proxy for that energy, at a discrete particle, i. The time average of an individual particle over the interval is

$$\varepsilon_i(t) = \frac{1}{t} \int_0^t E_i\left(t'\right) dt'. \qquad (1)$$

For this particular application of the TM metric, we use $E_i(t) \equiv \psi_i(t)$, the number of events greater than some minimum magnitude cutoff, M_{cutoff}, calculated for each year. Specifically, we specify for each region or subregion under analysis in each tectonic zone a grid, or set of boxes, that we will use to separate our seismic events by location, designated by i. For each box we count the number of seismic events to occur during a specific time period which, for all subsequent analyses discussed here, is set at one year. This is our seismicity rate, $\psi_i(t)$, or number of events for each year at each location i. As detailed in FERGUSON et al. (1999) and TIAMPO et al. (2007), for our purposes in calculating the TM metric and its inverse, $\psi_i(t)$ is a proxy for energy, and substituted for $E_i(t)$ in equation (1), above.

The ensemble average of those temporal averages over N particles of a system in the same time interval is

$$\bar{\varepsilon}(t) = \frac{1}{N} \sum_{i=1}^{N} \varepsilon_i(t). \qquad (2)$$

The Thirumalai–Mountain fluctuation metric, $\Omega_e(t)$, is defined as

$$\Omega_e(t) = \frac{1}{N} \sum_{i=1}^{N} [\varepsilon_i(t) - \bar{\varepsilon}(t)]^2. \qquad (3)$$

From Equation (3), the TM metric is the spatial variance of the temporal averages over all particles in the same time interval. THIRUMALAI et al. (1989) showed that, for an effectively ergodic system, the inverse of the fluctuation metric will grow linearly with time. This behavior is related to the central limit theorem, where the variance becomes a constant controlled by the large sample size N and divided by the increasing time t. Therefore

$$\Omega_e(t) = \frac{D_e}{t}, \qquad (4)$$

where D_e is related to the rate at which the phase space is explored, and can be used to calculate the time to reach effective ergodicity, τ_e, where $\tau_e \approx 1/D_e$ (THIRUMALAI et al., 1989; MOUNTAIN and THIRUMALAI, 1992). As noted above, in this research, the number of earthquakes greater than a given magnitude, m, is adopted as a proxy for energy release (TIAMPO et al., 2007). The expected linearly increasing relationship between the inverse TM metric and time was obtained in both simulated and natural earthquake fault systems (FERGUSON et al., 1999; TIAMPO et al., 2003, 2007). Specifically, TIAMPO et al. (2003, 2007), showed that, for California seismicity between 1932 and the present, the inverse TM metric is piecewise linear for particular realizations of boxsize discretization and minimum magnitude cutoff, allowing for the identification of regions of punctuated ergodicity in which the seismicity rate, for those particular parameter values, was stationary.

2.2. Pattern Informatics Index

The PI index is an analytical method for quantifying the spatiotemporal seismicity rate changes in historic seismicity (RUNDLE et al., 2002; TIAMPO et al., 2002; HOLLIDAY et al., 2006a). The quantitative basis for this technique lies in phase dynamics analysis, where the temporal evolution of a dynamical quantity is described by changes in the amplitude and phase angle of a state vector (HOLMES et al., 1996; MORI and KURAMOTO, 1998; RUNDLE et al., 2000). By integrating these rotations over time and differencing them at various observation times, space–time patterns of anomalous activity or quiescence emerge that seem to precede large events. Analysis supports the interpretation that the evolution of these seismicity patterns is the surface expression of changes in the underlying stress level, where smaller seismicity is acting as a sensor, responding to and illuminating locations of stress change prior to large events (TIAMPO et al., 2006a). The spatial locations of these coherent structures can be related to the locations of large earthquakes that occur a few years after their formation, and appear to have some forecasting capability (TIAMPO et al., 2002, 2006a; HOLLIDAY et al., 2006a).

To calculate the PI index in natural catalogs, seismicity data are taken from existing observations in seismically active areas. In order to ensure that all the data are consistent with the completeness of the catalog, a minimum magnitude cutoff, M_{cutoff}, is imposed on the natural catalogue. The time period for analysis and magnitude cutoff is related to the fact that the PI analysis uses numbers of events, and relies on changes in the relatively large numbers of smaller earthquakes as a proxy for stress change (DIETERICH, 1994; DIETERICH et al., 2000; TODA et al., 2002; TIAMPO et al., 2006a). The data are discretized by location into coarse-grained grid boxes. A gridding boxsize of 0.1 degrees, latitude and longitude, has proven successful in California, but may not be applicable in all tectonic areas. Time series are created for each of these gridded locations, where an individual time bin represents the total number of events at each location that occurred during that time step. Each location is denoted x_i, where i equals 1 to N locations.

We define the observed seismic activity rate $\psi_{\text{obs}}(x_i,t)$ as the number of earthquakes per unit time, $M \geq M_{\text{cutoff}}$, within the box centered at x_i at time t. In the following analysis the time period will be one year, so that $\psi_{\text{obs}}(x_i,t)$ is the number of events per year. We then define the time-averaged seismicity function $\mathbf{S}(x_i,t_0,t)$ over the interval $(t - t_0)$:

$$\mathbf{S}(x_i, t_0, t) = \frac{1}{(t - t_0)} \int_{t_0}^{t} \psi_{\text{obs}}(x_i, t)\, \mathrm{d}t. \qquad (5)$$

There are N locations for $\mathbf{S}(x_i,t_0,t)$. Denoting spatial averages over the N boxes by $\langle \rangle$, the phase function $\mathbf{S}'(x_i,t_0,t)$ is then defined to be the mean-zero, unit-norm function obtained from $\mathbf{S}(x_i,t_0,t)$:

$$\mathbf{S}'(x_i, t_0, t) = \frac{\mathbf{S}(x_i, t_0, t) - \langle \mathbf{S}(x_i, t_0, t) \rangle}{\|\mathbf{S}(x_i, t_0, t)\|}, \qquad (6)$$

where $\|\mathbf{S}(x_i,t_0,t)\|$ is the square root of the variance (the standard deviation) calculated for all spatial boxes.

Dividing by the constant variance normalizes the seismicity to its background and illuminates small, local variations in seismicity. Changes in seismicity are given by $\Delta\mathbf{S}'(x_i,t_1,t_2) = \mathbf{S}'(x_i,t_0,t_2) - \mathbf{S}'(x_i,t_0,t_1)$. The physical picture is that $\Delta\mathbf{S}'(x_i,t_1,t_2)$, the local change in seismicity rate, identified by the relative change in spatial and temporal seismic activity, is related to the underlying stress changes in the system. $\Delta\mathbf{S}'(x_i,t_1,t_2)$ will be positive or negative, depending on whether it is identifying seismic activation or quiescence (TIAMPO et al., 2002, 2006b). In the final calculation, $\Delta\mathbf{S}'(x_i,t_1,t_2)$ is averaged over all possible base years, t_0, in order to reduce the effects of noise in the seismic catalog. Note that the calculation of $\mathbf{S}'(x_i,t_0,t)$ and, therefore, $\Delta\mathbf{S}'(x_i,t_1,t_2)$, is a function of both the long-term mean and spatial variance of the background seismicity rate. As a result, accurate calculation of $\Delta\mathbf{S}'(x_i,t_1,t_2)$ is dependent on constant long-term averages, or stationarity.

The PI index, $\Delta\mathbf{P}$, is related to the power in $\Delta\mathbf{S}'(x_i,t_1,t_2)$. $\Delta\mathbf{P} = \Delta\mathbf{P}(x_i,t_1,t_2) = \{\Delta\mathbf{S}'(x_i,t_1,t_2)\}^2 - \mu_{\text{p}}$. μ_{p} is the spatial mean of $\{\Delta\mathbf{S}'(x_i,t_1,t_2)\}^2$ and represents the time-dependent background. For any given catalog, it is possible to compute the power in the relative change in seismicity over any given time period using the PI index.

In recent years, the PI technique has been applied to California seismicity for the purpose of identifying systematic space–time variations in seismicity that are a measure of current and future seismic moment release (TIAMPO et al., 2002). These variations, or anomalies, objectively identify regions where the local stress variations result in anomalous seismicity changes at a location x, during a time interval, $t_2 - t_1$ (TIAMPO et al., 2006a). For example, the PI index has been used to identify stress shadows associated with the small but persistent changes in seismicity associated with large events in southern California (TIAMPO et al., 2006b). In addition, given that the spatiotemporal variations in seismicity related to underlying stress change serve to identify precursory activity prior to large earthquakes, the PI method has been tested and shown to be a reliable method for forecasting these upcoming events (HOLLIDAY et al., 2006a). HOLLIDAY et al. (2006a) also demonstrated that ongoing studies of this forecast methodology suggest that the PI index represents a threshold probability, in which a value may be chosen above which there is 100% expectation of a large event.

3. Analysis

The results in 2.1, above, suggest that for particular ranges of the important spatial and temporal

parameters the statistical averages of the seismic fault system are stationary, and the spatial averages can be substituted for the temporal averages, and vice versa. In addition, it implies that, for some measurable and significant period of time, the system is in equilibrium. This has potential implications for earthquake forecasting, as many seismicity-based forecasting methods, such as the PI index, rely on identifying variations in the seismicity relative to some quantifiable measure of what is considered the longer-term, averaged behavior of the system. In addition, many of these methods rely on some type of linear behavior of the system in their forward projections. Our hypothesis is that the TM metric can be used to identify those spatial and temporal regions of the seismic catalog that will provide better seismicity-based forecasts.

The PI index, in particular, relies on both of the above assumptions (RUNDLE *et al.*, 2000, 2002; TIAMPO *et al.*, 2002). Specifically, as can be seen in equation (6), above, the PI index uses both the spatial mean and variance in its calculation. If either the mean or the variance fluctuates too much over time, the estimate of the relative fluctuation in the seismicity will be inaccurate. Therefore, it should be possible to optimize, or at the very least improve, PI forecasts for various natural historic catalogs using the TM metric to identify the ergodic limits of the spatial and temporal parameters that factor into its calculations and to test the above hypothesis. Specific parameters affecting the ergodic behavior are the time period and spatial range of the analysis, the grid boxsize, and the minimum magnitude cutoff. In the following sections, we will present results from eastern Canada and Taiwan.

3.1. Natural Catalogs

3.1.1 Eastern Canada

The eastern Canadian shield is an intraplate tectonic region in which most of the earthquake activity is associated with lithospheric-scale geological structures arising from past orogenic and rifting episodes, and these appear to control the spatial distribution of its seismicity (ADAMS and BASHAM, 1989). Figure 1 shows the regional seismicity between 1903 and the
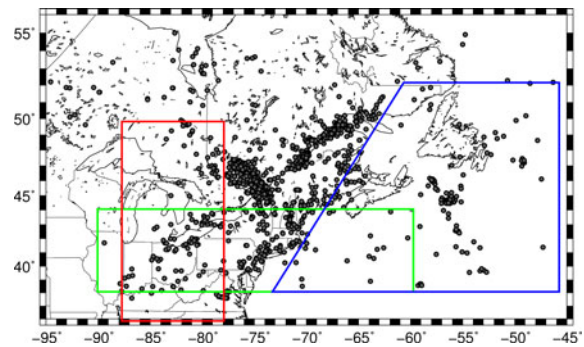

Figure 1
Seismicity in northeastern U.S. and southeastern Canada from 1903 to 2002, $M \geq 2.5$. The three subregions used for testing the spatial heterogeneity of the catalog completeness are outlined by the *blue* (subcatalog 1), *red* (subcatalog 2), and *green* (subcatalog 3) *polygons*. SHEEF catalog courtesy of S. Halchuck and J. Adams, GSC

present. Three subregions used for testing the spatial heterogeneity of the catalog completeness are outlined by the blue (subcatalog 1), red (subcatalog 2), and green (subcatalog 3) polygons. Activity varies from low-level background seismicity to moderate $(4 \leq M \leq 6)$ and rare large (magnitude $M \sim 7$) earthquakes. The bulk of the seismicity occurs within the top 25 km of the crust (ADAMS and BASHAM, 1989).

The data used here come from the Seismic Hazard Earthquake Epicentre File (SHEEF) catalog, compiled by the Geological Survey of Canada. The original catalog includes all located events of magnitude 2.5 or greater reverting to 1627. The magnitudes given in the catalog are Nuttli magnitudes (M_N), a body-wave magnitude scale. We tested the completeness of the catalog by calculating the Gutenberg-Richter frequency–magnitude statistics for approximately 20-year-long catalog intervals from 1900 through 2002. For each time window, we apply a least-squares fitting routine to the frequency data for a range of minimum magnitudes. We then calculate the root-mean-square (RMS) error of the fit associated with each minimum magnitude. Finally, we assign a minimum magnitude of completeness (MC) to the time window based on a combination of the lowest RMS error and visual inspection of the data (Table 1). The results indicate that the catalog is complete above magnitude 3.0 back to 1950; however the seismicity is clustered

Table 1

Frequency–magnitude statistics for the SHEEF catalog

Years	*a*-value	*b*-value	RMS	Mc
Full catalog				
1900–1920	2.874	0.435	0.031	4.5
1930–1950	5.467	0.903	0.049	4.3
1950–1970	5.531	0.997	0.076	3.0
1960–1980	5.581	1.021	0.058	2.9
1970–1990	5.206	0.868	0.064	2.5
1980–2002	5.543	0.920	0.072	2.5
Subcatalog 1				
1950–1970	2.180	0.356	0.044	3.6
1960–1980	3.791	0.736	0.064	3.5
1970–1990	5.207	1.048	0.077	3.2
1980–2002	5.573	1.130	0.084	3.2
Subcatalog 2				
1950–1970	4.993	1.038	0.061	2.9[a]
1960–1980	7.119	1.642	0.125	3.1[a]
1970–1990	5.575	1.197	0.074	2.9[a]
1980–2002	5.503	1.208	0.066	2.9[a]
Subcatalog 3				
1950–1970	3.985	0.795	0.038	2.9
1960–1980	4.612	1.010	0.087	2.9
1970–1990				2.9[b]
1980–2002	5.832	1.355	0.066	2.9[a]

Least-squares fitting is used to determine the minimum magnitude of completeness (Mc) for each time period. Three spatial subcatalogs are also tested

[a] Least-squares fitting was only applied to the events of $M \leq 4.0$ due to the paucity of larger events

[b] Based on visual inspection. The fitting algorithm could not be applied due to a lack of $M > 3.5$ events

centrally in the region, suggesting that the spatial coverage of the network is heterogeneous. We repeated the above analysis for the Atlantic off-shore seismicity (Fig. 1, subcatalog 1), the western edge of the catalog (Fig. 1, subcatalog 2) and the southern portion containing the U.S. activity (Fig. 1, subcatalog 3). The results, summarized in Table 1, suggest that the off-shore coverage is very poor, even in recent years. However, the southern and western subcatalogs appear to be complete above magnitude 2.9 from 1950 onwards, with only a slight, questionable decrease in the completeness for the western boundary for the period 1960–1980. To further confirm these results, we calculated the cumulative number of events of $M \geq 3.0$ region-wide as a function of time (not shown here). The data are distinctly linear, with no noticeable changes in slope. As a result, for this analysis, calculations are limited

to the area between 42° to 52° latitude and −60° to −85° longitude. However, it should be noted that the a-value does increase over time in all subregions, as seen in Table 1, which is a result of the increase in number and quality of the networks over time (personal communication, Dr. R. Mereu). This is confirmed with a calculation of the average number of events per year of $M \geq 3$. While in the first half of the century there are significant jumps in rate, followed by periods of constant production, a sudden increase in the early 1980s is followed by a steady rise in the rate of events per year. This effect is almost nonexistent for $M \geq 4$.

Figure 2 shows the normalized inverse TM metric for eastern Canada, 1903–2001 and boxsize equal to 0.2 degree. Other boxsizes were tested (not shown), however, there was no significant improvement at smaller sizes. In Fig. 2a, calculated for $M \geq 3.0$, there are no periods in which the inverse TM metric appears linear, and after the mid-1970s it begins to curve downward and continues to do so throughout the 1990s, until the present. Figure 2b shows a plot for $M \geq 3.0$, 1970–2001. The inverse TM metric in eastern Canada, $M \geq 3.0$, for 1970–2001 is not linear, or piecewise linear, but continues to maintain its downward curve after 1985. Our interpretation here is that this is associated with the increase in number of events of $M \geq 3.0$ per year that is seen over that same period.

In Fig. 2c, now calculated for $M \geq 4.0$ and 1903–2001, the inverse TM metric displays linear behavior for periods prior to 1980, followed by a change in the average slope and a subsequent piecewise linear behavior. Figure 2d shows the same metric, $M \geq 4.0$, but for the time period 1970–2001. Here the behavior is primarily linear, with a constant slope.

The PI index, ∆**P**, calculated for eastern Canada for the period 1995 to 2000, inclusive, is shown in Fig. 3. Here the gridded boxsize is again 0.2 degrees. Using the interpretation of HOLLIDAY et al. (2006a), we assign a threshold probability of zero to the PI index, in which any location with a value of ∆**P** > 0 is chosen such that there is 100% expectation of a large event, and is subsequently colored red. Figures 3a and 3b are ∆**P** for $M \geq 3.0$ and $M \geq 4.0$, respectively. Inverted triangles represent events of $M \geq 4.0$ during the period 1995–2000
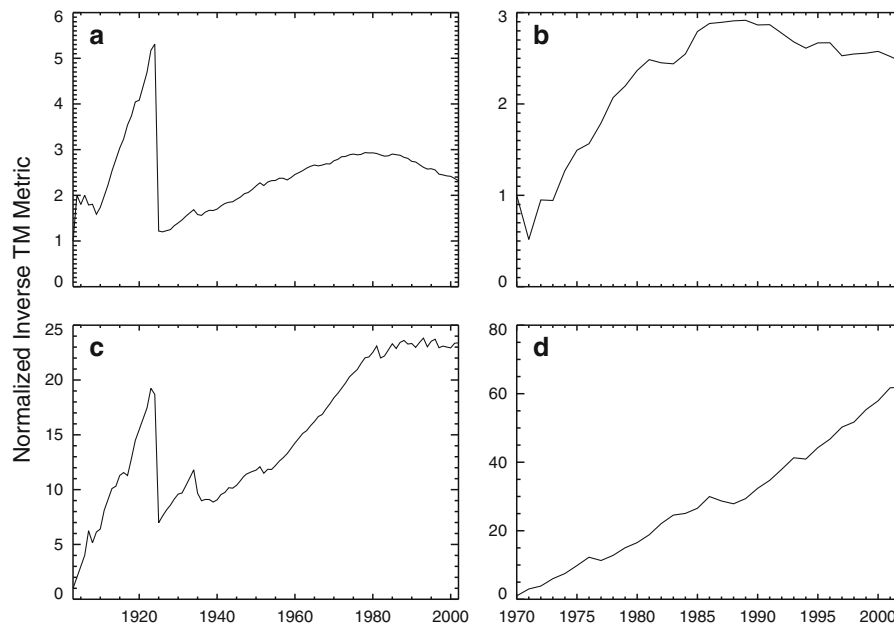
Figure 2
Normalized inverse TM metric for eastern Canada, 1903–2001 and boxsize = 0.2 degree: (**a**) $M \geq 3.0$, 1903–2001; (**b**) $M \geq 3.0$, 1970–2001; (**c**) $M \geq 4.0$, 1903–2001 and (**d**) $M \geq 4.0$, 1970–2001

(inclusive), while circles represent those events of $M \geq 4.0$ that occurred between 2001 and the present.

Relative operating characteristic (ROC) diagrams were computed in order to compare the performance of the results shown in Fig. 3. In an ROC diagram, the hit rate, H, is plotted versus the false alarm rate, F. Details of the ROC diagram computation can be found elsewhere (JOLLIFFE and STEPHENSON, 2003), but the calculation is designed to ensure that if the area under the ROC curve is larger, the forecast is better (HOLLIDAY *et al.*, 2005). A random forecast will generate a straight line along the diagonal of an ROC plot. A more stringent null hypothesis for comparison of forecast results is the Relative Intensity (RI) index, as described in HOLLIDAY *et al.* (2006b). Relative intensity is defined as the long-term average seismic rate for each location during the time period from t_0 to t_2, and is a measure of historical seismicity. As such, it provides a reasonable null hypothesis to test against the PI index. Here, a forecast is successful (i.e., a hit) if the epicenter of the earthquake lies within a hotspot box or in one of the eight adjoining boxes (MOORE, 1962).

Figure 4 shows ROC diagrams for the PI maps shown in Fig. 3. The PI calculation is shown in blue,

the RI calculation is shown in red. Figure 4a shows the ROC diagram for PI and RI calculations for $M \geq 3$, a forecast time period of 2001 through 2006 (inclusive) and events of $M \geq 4.5$. Figure 4b shows the same calculation, but for $M \geq 4$. Here the ROC plots in Fig. 4 only include values for $F = [0,0.5]$. For $F > 0.5$, the PI and RI plots are virtually indistinguishable, as the PI forecast begins to approach the RI forecast. In addition, the implication of effective binary forecasting implies that any forecast with a high false alarm rate will result in too many false positives for practical application.

Comparing these figures, it is clear that the forecast in Fig. 3a, $M \geq 3.0$, has a significantly higher false positive rate than Fig. 3b, although with approximately the same number of successful forecast events. In contrast, the forecast for $M \geq 4.0$, Fig. 3b, has a much lower false positive rate and the same amount of false negatives. The ROC diagrams in Fig. 4 support this result. In Fig. 4a, the RI index performs better than the PI index for the forecast of Fig. 3a, while the PI index is significantly improved in Fig. 3b. The ROC diagram of Fig. 4b shows that the PI index is above the RI index, because the PI index has a lower false positive rate, as seen in
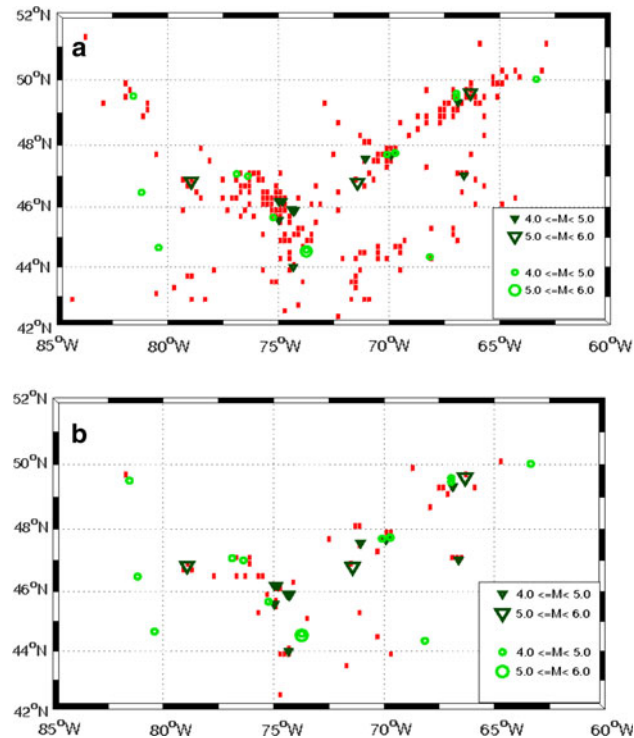
Figure 3

PI index, ΔP, for eastern Canada for the period 2000–1991 (inclusive), and a boxsize = 0.2 degrees. Here *red boxes* indicate all locations where ΔP > 0. ΔP is shown for (**a**) $M \geq 3.0$ and (**b**) $M \geq 4.0$. *Inverted triangles* represent events of $M \geq 4.0$, scaled with increasing magnitude, during the period 1995 through the end of 2000, while *circles* represent those events that occurred between 2001 and 2006 (inclusive)

Fig. 3b. The Pierce Skill Score (PSS) (JOLLIFFE and STEPHENSON, 2003), the integrated area under the complete ROC curves, supports this result, where the PSS for the PI index is greater than that of the RI index in Fig. 4b.

This analysis supports the hypothesis that configuration of the PI index calculation in accordance with the effectively ergodic regimes as delineated by the TM metric can improve its forecasting accuracy. It should be pointed out that this particular result is not surprising, in light of what is known about this particular network and the details of the PI calculation. If the apparent seismicity rate increases over time (in this case $M \geq 3.0$), then the PI index will calculate that as an increase in activation over any time difference during that period. PI anomalies will be interpreted incorrectly as false positives, as seen in Fig. 3. In this case, ensuring that the system is ergodic over a particular time period ensures that the background rate is stationary; an assumption implicit

in the formulation of the PI method and a requirement for an accurate evaluation.

3.1.2 Taiwan

Taiwan is situated on the western portion of the Pacific Rim, along the Ryukyu subduction zone. East of the island the leading edge of the Pacific plate subducts under the Philippine Sea plate, while on the western side the Philippine Sea plate subducts below the Eurasian plate. South of the island, the South China subplate subducts under the Philippine Sea plate. Finally, on the southeast portion of Taiwan, the Eurasian and Philippine Sea plate suture zone separates the region into two separate tectonic provinces (Wu *et al.*, 2008). As a result of significant compression across the island, Taiwan has a relatively high seismic activity rate with a significant depth component.

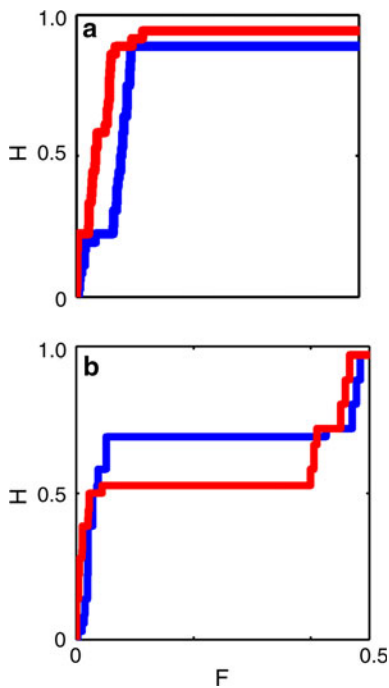The seismicity data employed in this research was the Taiwanese Central Weather Bureau (CWB)

Figure 4

ROC diagrams for the PI maps shown in Fig. 3. The PI calculation is shown in *blue*, the RI calculation is shown in *red*. In **a** is shown the ROC diagram for PI and RI calculations for $M \geq 3$, a forecast time period of 2001 through 2006 (inclusive), and a forecast for events of $M \geq 4.5$. In **b** is shown the same calculation, but for PI and RI calculations of $M \geq 4$

Figure 5

Seismicity map, $M \geq 3$, for Taiwan, from the CWB seismic network catalog

catalog from 1 January, 1973 to 31 December, 2006, shown in Fig. 5. The research region was $21°$ to $26°$ latitude, $119°$ to $123°$ longitude. Spatial variation of Mc for the entire catalog was computed using the maximum curvature method (WIEMER and WYSS, 2000; WIEMER, 2005). The catalog generally appears to be complete for $M \sim 3$ for the entire region, with the exception of some off-shore areas to the south and east with relatively little seismic activity or poor network coverage. Nevertheless, temporal catalog homogeneity, rather than a static spatial variation of M_{cutoff}, is particularly important for PI studies. While time series of M_{cutoff} maps can be computed, this is a cumbersome, time-consuming process that is strongly dependent on the choice of time step. Therefore, an evaluation of the catalog's homogeneity was performed using the method of HABERMANN (1983).

Results from the application of Habermann's test of catalog homogeneity (HABERMANN, 1983; WIEMER, 2005) for the Taiwanese catalog suggest that times of
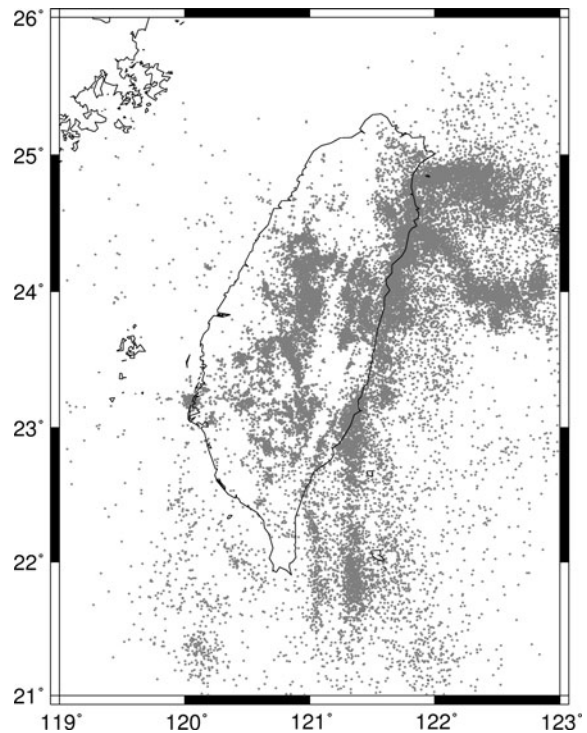
apparent seismicity rate increases (for magnitude bands with negative Z values) and rate decreases (for magnitude bands with positive Z values) are identified at the 0.01 significance level based on the assumption that all samples derive from asymptotically probable standard Gaussian distributions. To offset limitations in this method, such as a lack of normality for short-time windows and sensitivity to variations in statistical properties (MARSAN 2003; MATTHEWS and REASENBERG, 1987), a catalog is often declustered with Reasenberg's algorithm (REASENBERG, 1985) before further analysis. Results after declustering appear to be affected by the artificial noise introduced in the declustering procedure, however. While there are no obvious magnitude shifts (HABERMANN, 1987), significant rate increases (likely due to detection level improvements) early in the catalog (pre-1980) and rate anomalies corresponding to large earthquake sequences do exist in the data. Again, while declustering by Reasenberg's algorithm is not appropriate for the Taiwanese subduction zone, whose tectonics and seismicity patterns vary significantly in

3-D, it is often included in the application of Habermann's test for catalog homogeneity (above) (e.g., WYSS and WIEMER, 1997), making the results for that analysis difficult to interpret.

In order to better understand the applicability of the declustering procedure, we performed a separate evaluation of the variation in energy, magnitude and number of events with depth and time, which we also applied to the declustered catalog (REASENBERG, 1985). This result suggests that there is an artificial clustering in depth, likely due to assigned default depths for inadequately located events, which remained after declustering. The declustering tool also did not clean the circa 1986 clusters, likely due to the inappropriate use of the windowing scheme. Catalog inhomogeneity is apparent for pre-1980s and for deep events over the entire catalog, likely due to the detection-level improvement of the observation network in both space and time. There is also an apparent decrease in the number of reported shallow events (< 3 km) since 1990, although this could be due to the improvement of event location accuracy.

Based on our previous research, we applied the TM method to the original data set, with no declustering applied, because an evaluation of stationarity will locate those regions in which both the spatial and temporal averages converge to constant values, making this methodology simpler to interpret than those attempted above. In addition, these stationary averages must approach the same value in order for the system to be ergodic (TIAMPO et al., 2007).

Figure 6 shows a number of inverse TM metric calculations for the Taiwanese subduction zone. As a result of the evaluation of the variation in energy, magnitude and number of events with depth and time detailed above, only events of $M \geq 3$ were used. The focal depth threshold adopted was 30 km to limit the effect of decreasing accuracy with depth. We implemented both a two-dimensional (2-D) and a three-dimensional (3-D) calculation of both the TM metric and PI calculations, in order to study the effect of seismic variations with depth. Figure 6a is a 2-D analysis of events of $M \geq 3$ and a gridding boxsize of 0.1°. Figures 6b and 6c are 3-D analyses, $M \geq 3$, but with a discretization of $0.1° \times 0.1° \times 1$ km and $0.1° \times 0.1° \times 0.25$ km, respectively. Figure 6d is

another 2-D analysis, but for $M \geq 4$ and a boxsize of 0.02°. Figures 6e and 6f are again 3-D analyses and a discretization of $0.1° \times 0.1° \times 1$ km and $0.1° \times 0.1° \times 0.25$ km, $M \geq 4$.

Here all of the plots except for Fig. 6a have periods of linear behavior after the mid-1980s. However, it is also clear that ergodicity improves with increasing magnitude and decreasing boxsize. It is also apparent that the 3-D analysis provides significantly better ergodic behavior than the 2-D analysis. Finally, Figs. 6a through 6f all show breaks in ergodicity related to events of $M \geq 5$, including the occurrence of the $M = 7.3$ Chi–Chi earthquake in 1999. One interesting point is that ergodic behavior is evident at small depth increments, where the accuracy is on the order of 4 km. This likely is a result of the central limit theorem, again, as the variance, or error, in location is reduced by averaging over many realizations. However, additional testing using synthetic catalogs with various noise levels will be necessary to confirm that this hypothesis is correct.

The TM method successfully evaluates the general homogeneity of the catalog both in space and time, while Habermann's test of catalog homogeneity was too sensitive and impractical for this catalog data, in part because of the necessity of declustering the catalog first. Note that this particular Habermann's test required almost two weeks for a full analysis (2-D only) on an Intel processor with 2.4 GHz CPU and 3 GB Memory, while the TM analysis takes minutes to hours, depending on whether a 2-D or 3-D computation is performed. For the specific purpose of determining which regions are stationary for forecasting applications, the TM method provides a clearer and simpler interpretation, and is also an efficient and accurate method for locating these regions.

A 3-D calculation of the PI index is shown in Fig. 7 for the ergodic time period, 1994–1998 and the parameters of Fig. 6c, i.e., $M \geq 3$, a unit time step of 1 year and a discretization of $0.1° \times 0.1° \times 0.25$ km. In addition, we have included plots for the RI index (HOLLIDAY et al., 2006b). In these figures, green circles indicate the large events of $M \geq 6$ that occur after the forecast period, 1999–2003. Figures 6a and 6b are for a depth range of 7.75–8.00 km, while Figs. 6c and 6d are for a depth range of 13.75–14.00 km. The color
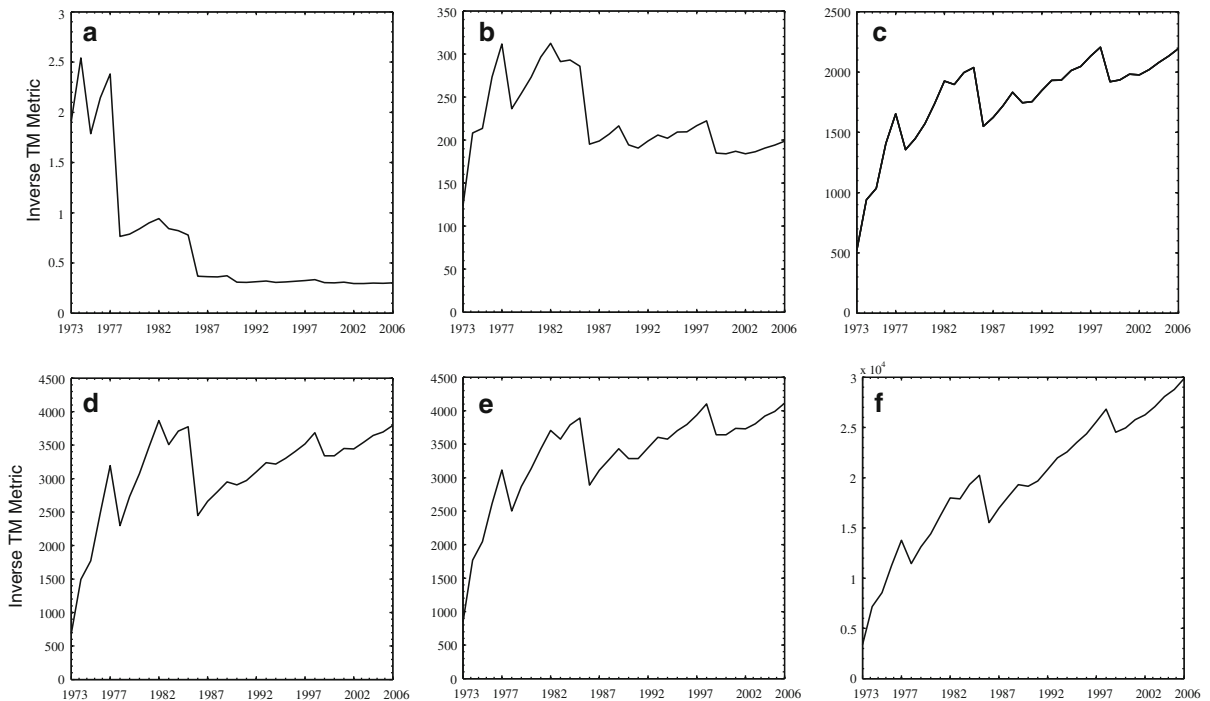
Figure 6

Plots of the inverse TM metric, unit time step of 1 year, for the Taiwanese subduction zone. **a** $M \geq 3$, 2-D analysis, and a gridding boxsize (coarse-graining discretization) of 0.1°; **b** $M \geq 3$, 3-D analysis, and a discretization of 0.1° × 0.1° × 1 km; **c** $M \geq 3$, 3-D analysis, and a discretization of 0.1° × 0.1° × 0.25 km; **d** $M \geq 4$, 2-D analysis, and a boxsize discretization of 0.02°; **e** $M \geq 4$, 3-D analysis, coarse-grained box is 0.1° × 0.1° × 1 km; and **f** $M \geq 4$, 3-D analysis, discretization of 0.1° × 0.1° × 0.25 km

scale is logarithmic, where the number represents the exponent. All values are normalized by the maximum values of each plot. Note that the PI index forecasts the location of all future events (green circles) in those depth ranges, including the Chi–Chi earthquake in Fig. 6a, as does the RI index, although with fewer false positives.

Figure 8 is also a 3-D calculation of the PI and RI indices, similar to that shown in Fig. 7, but for the *nonergodic* time period 1988–1997. Here the inverse TM metric shows a significant break in 1992 (Fig. 6c). Here, while the RI index continues to forecast the events post-1998, in addition to a numerous false positives, the PI index fails to forecast the same events, although it still limits false positives to a small percentage.

Figure 9 quantifies the difference in performance of these two forecasts (1994–1998 and 1988–1997). ROC diagrams were computed in order to compare the performance of the 3-D PI calculation for the entire depth range for the two different time periods.

Here, again, the F axis is shortened to $F < 0.3$. In Fig. 9a, for the ergodic time period 1994–1998, the curve of the PI map remains significantly above that of the RI map until their intersection at approximately 0.25 on the horizontal axis, illustrating that the PI map provides a better forecast than the RI map for this case. However, in Fig. 9b, we see that while the performance of the RI index is remarkably stable for long-time periods, and varies little whether the system is ergodic or nonergodic, the performance of the PI index is significantly poorer for the nonergodic time period. For those ergodic cases tested to date, the PI index outperforms the RI index, primarily because the RI index does not identify quiescence. These results again support the hypothesis that PI index forecasts can be improved significantly by restricting the important parameters of the calculation to those associated with ergodic behavior.

However, the above test is different from that of eastern Canada. In eastern Canada, the ergodic calculation is an improvement over the nonergodic
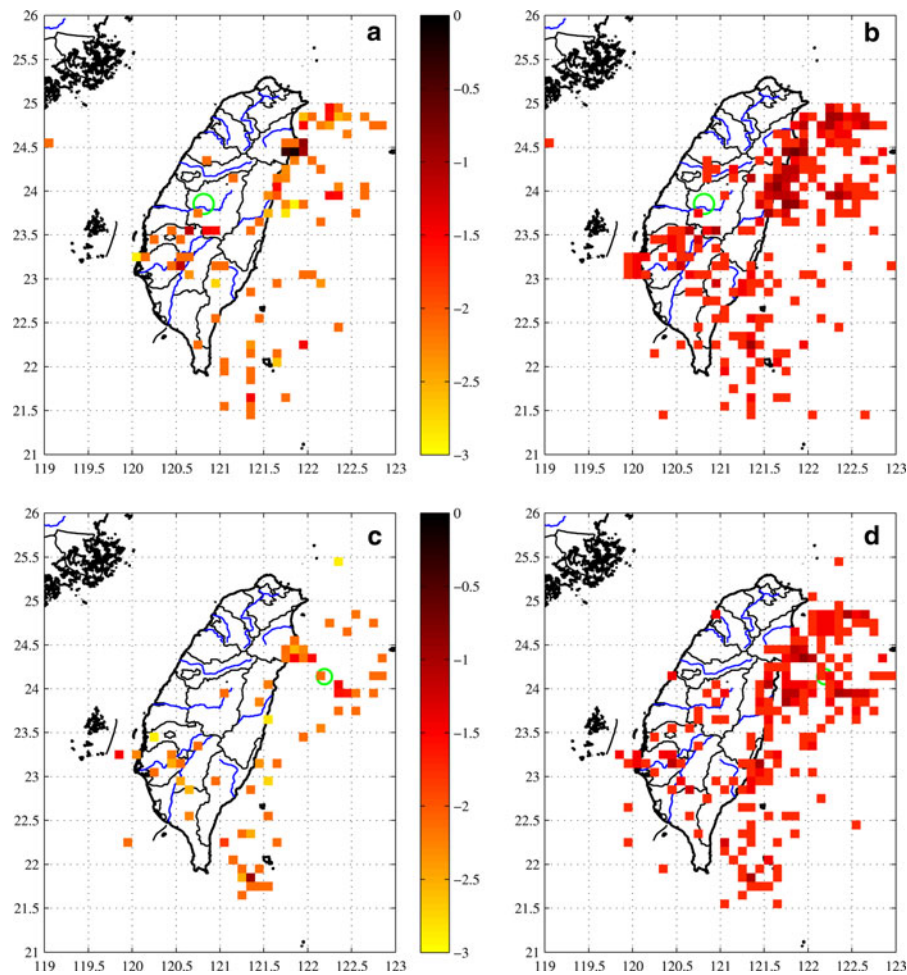
Figure 7

Plots of 3-D PI and RI maps the Taiwanese subduction zone for varying depth ranges. The analysis corresponds to those parameters used for Fig. 6c; i.e., $M \geq 3$, a unit time step of 1 year, and a discretization of $0.1° \times 0.1° \times 0.25$ km. The forecast period is 1994–1998. *Green circles* indicate the large events which $M \geq 6$ that occur in the period 1999–2003. Depth ranges of **a** and **b** 7.75 to 8.00 km, **c** and **d** 13.75 to 14.00 km. The *color scale* is logarithmic, where the number represents the exponent. All values are normalized by the maximum values of each plot

calculation because it reduces the number of false positives but still forecasts the same number of events; i.e., there are no additional misses. In the case of Taiwan, the false positive rate is the same for the nonergodic and ergodic time periods; it is an increase in misses that apparently degrades the forecast for the nonergodic time period. This suggests that the cause of the nonergodic behavior may be different in these examples.

The above analysis for natural catalogs provides evidence that the occurrence of large events and their aftershock sequences associated with these breaks in

ergodicity are affecting the ability of the PI index to detect precursory quiescence patterns. This possibility, and potential mechanisms for its occurrence, is investigated using synthetic catalogs in Section 3.2.

3.2. Synthetic Seismicity Catalogs

In a preliminary attempt to better understand the behavior of the PI index and potentially other linear forecasting algorithms based on historic seismicity, we studied synthetic seismicity catalogs that were formulated to match the statistics of natural
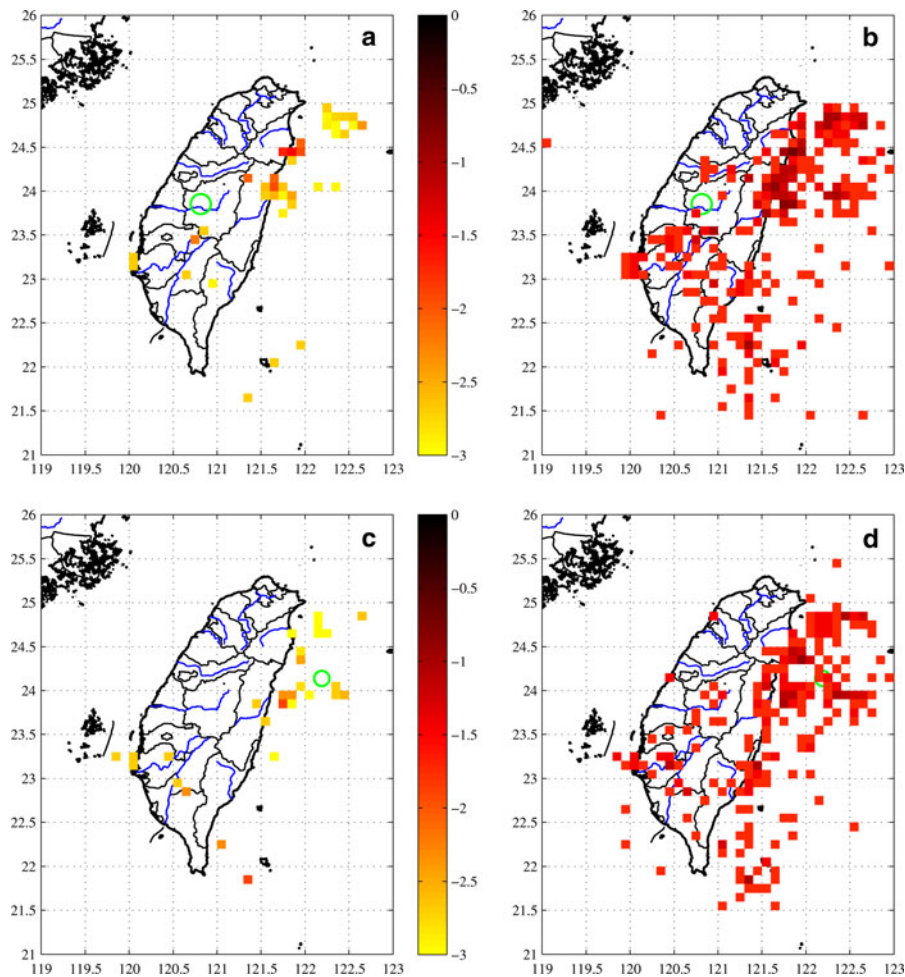
Figure 8
Plots of 3-D PI and RI maps with parameters as shown in Fig. 6c, but for the forecast period of 1988–1997. *Green circles* indicate the large events which $M \geq 6$ that occur in the period 1998–2006. Depth ranges of **a** and **b** 7.75 to 8.00 km, **c** and **d** 13.75 to 14.00 km. The *color scale* is as seen in Fig. 7, above

seismicity catalogs. While these synthetic catalogs are only a simplification of the natural earthquake process, a first step toward a more detailed set of synthetic catalogs, in this case we have included an additional signal reminiscent of those hypothesized to act as precursors to larger events in order to study one potentially quantifiable precursory signal, anomalous quiescence. This particular precursory seismic pattern, based upon Non-Critical Precursory Accelerating Seismicity Theory (or Non-Critical PAST), recently was proposed to explain the formation of accelerating seismicity that may be observed before large earthquakes (MIGNAN, 2008a). In this particular formulation, physically realistic catalogs

with activation and quiescence are formulated that depend on only two input parameters: the regional events rate and the noise level in the theoretical precursory signal. In recent work (MIGNAN and TIAMPO, 2010), it was shown that the PI index is successful at identifying the anomalous quiescence associated with the Non-Critical PAST phenomena.

Non-Critical PAST is based upon the hypothesis that Accelerating Moment Release (AMR) occurs, in a significant number of cases, prior to the occurrence of large events. AMR is typically modeled by a simple power-law time-to-failure equation (BUFE and VARNES, 1993), defined by the relation is
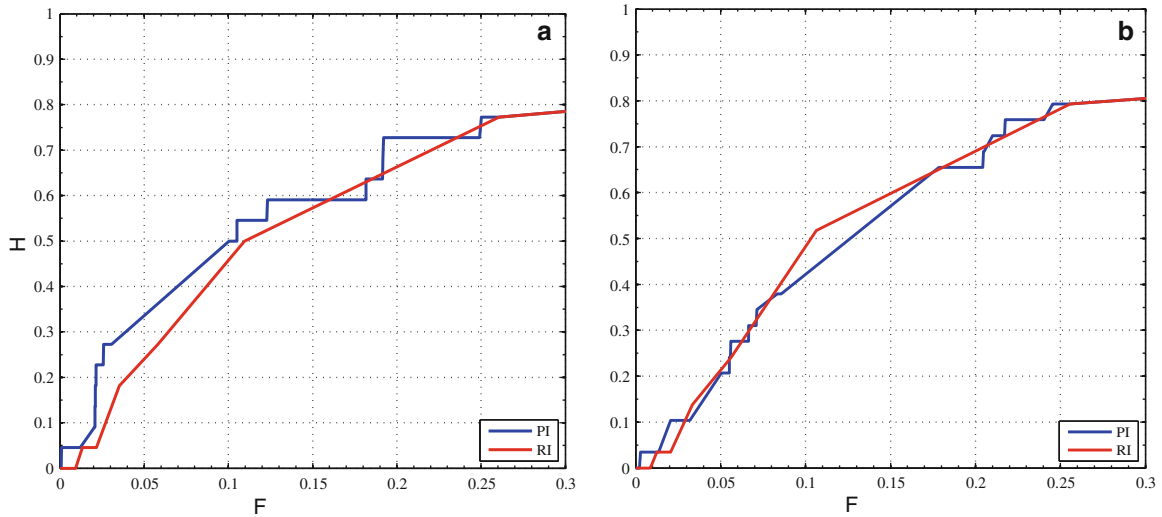
Figure 9
ROC diagrams for the PI and RI maps shown in Figs. 7 and 8. On the *left* is shown the ROC diagram calculated for the ergodic time period, 1994–1998, of Fig. 7. On the *right* is shown the ROC diagram corresponding to the nonergodic time period, 1988–1997, of Fig. 8. *Key* is as shown on plots

$$\varepsilon(t) = A + B(t_f - t)^m, \qquad (7)$$

where t_f is the time of the main shock, and A, B and m are constants. Originally, and in subsequent work, $\varepsilon(t)$ was chosen to be the cumulative Benioff strain (BOWMAN *et al.*, 1998; BREHM and BRAILE, 1998; ZÖLLER *et al.*, 2000; PAPAZACHOS *et al.*, 2007) but recent work suggests that the cumulative number of events is preferable (JIMÉNEZ *et al.*, 2005; MIGNAN *et al.*, 2007). Because the cumulative number of events is a quantity directly input into the PI index, the relative effects of quiescence and activation should be quantifiable using this particular measure.

In Non-Critical PAST, the earthquake cycle is formulated using simple geometrical and stress transfer concepts, and physically-based synthetic catalogues can be constructed in order to test existing forecasting techniques and to understand how they react to different seismicity characteristics (MIGNAN, 2008a). A spatiotemporal distribution of background seismicity exists, surrounding and incorporating the stress field of a loading fault. At $t = 0$, a large earthquake occurs on the fault and creates a stress shadow which, for some period of time, appears as anomalous quiescence. The size of the stress shadow decreases through time, due to loading at depth, until it finally disappears at $t = t_f$ prior to the occurrence

of new large event (i.e., the expected main shock). Note, here, that this is not a complete catalog in that there is only one event that can be forecast, the large ($M \sim 7$) event at the end of the sequence.

Following MIGNAN et al. (2007), the density of events that composes the background seismicity is δ_b^0 outside the stress shadow and δ_b^- inside the stress shadow, with $\delta_b^0 > \delta_b^-$. If the spatiotemporal limits of the stress shadow are defined by a power law time-to-failure relation as in equation (7), the cumulative number of events $\psi(t)$ that comprise the background seismicity increases as a power-law function through time before the main shock, $\psi(t) \propto -(t_f-t)^{D/3}$, where D is the fractal dimension of the associated fault network (MIGNAN *et al.*, 2007). Note, again, that Non-Critical PAST also quantifies precursory quiescence similar to the seismicity pattern commonly known as a Mogi Doughnut (MOGI, 1969, 1977, 1979).

Theoretical synthetic catalogues for this study were created based on the above principles of the Non-Critical PAST. In order to form a precursory accelerating seismicity pattern based on an increase of the a value, only the location and time of background events must be included (MIGNAN *et al.*, 2007). Efforts to include magnitude information and aftershock clustering were implemented in addition to the standard formulation.

The background seismicity density δ_b^0 and the noise ratio δ_b^-/δ_b^0 are adjustable parameters, depending respectively on the regional seismic activity and on the effect of the stress shadow on seismicity. In this study, δ_b^0 is fixed to 1000 background events in the catalog per year. This corresponds to 0.008 events/degree^2/day in a 2000×2000 km square grid. The noise level, δ_b^-/δ_b^0 is set at 0.1. The location of background events and the time of occurrence are controlled by the stress contour limit $\sigma^*(x,y,t)$. The stress field $\sigma(x,y,t)$ is calculated for a thrust fault ($L = 200$ km, $W = 10$ km, dip = 45°) located in the center of a grid of 2000×2000 km. The time interval is [$t_0 = 0$; $t_f = 20$ year]. For each time step of one year, background events have a uniform random distribution in space and time with a density δ_b^0 outside the stress contour $\sigma^*(x,y,t_i)$ and δ_b^- inside the stress contour $\sigma^*(x,y,t_i)$. Coulomb stress calculations are performed with the source code AlmondX (courtesy of G.C.P. King) (OKADA, 1992). The stress field $\sigma(x,y,t_i)$ results from a displacement on the fault at t_0, producing a stress shadow which then decreases through time from the linear superposition of a loading stress field using the back-slip model concept (SAVAGE, 1983). The fault is ready to fail at the end of the catalogue, with a coupled precursory quiescence and activation seismicity pattern defined over the entire 20 year time frame (MIGNAN et al., 2007).

Background events are implemented randomly in space and time from a Gutenberg-Richter relation with a b value of 1.0 (GUTENBERG and RICHTER, 1944). The only anticipated main shock after the end of the catalog is the only event preceded by Non-Critical PAST seismicity. Here, the length and width are fixed, and the magnitude of the upcoming event is calculated from the relationship $M \sim 4 + \log(L^*W)$.

The minimum magnitude of background events is fixed at $M_{min} = 1.0$, to ensure that, for the density of events in the catalogue, the maximum magnitude M_{max} for the region is less than 6.0. This corresponds to an a value of approximately 4.4, lower than in many active seismic regions (e.g., $a \sim 6$ in California), while a minimum magnitude $M_{min} = 1.0$ also is artificial when compared to actual catalogues. This artificial value is due to the fact that these synthetic catalogues simulate the preparation process of only one large earthquake. However, all background events have the same weight independent of their magnitudes, consequently it is the density of background events ($\sim \delta_b^0$) that is similar to the actual catalogues, not the magnitude window.

Spatiotemporal clustering is included in the simulated background seismicity by following the Epidemic Type Aftershock Sequence Model (ETAS) model (e.g., OGATA, 1992; OGATA and ZHUANG, 2006). ETAS describes ordinary seismic activity $\lambda(t)$ by the superposition of a constant rate for background seismicity, μ, and the aftershock sequence of any given event j at time t_j, such that

$$\lambda(t) = \mu + \sum_{\{j:t_j<t\}} e^{\alpha(Mj-Mc)} \nu(t - t_j). \qquad (8)$$

In this case, the ETAS background rate, μ, is not constant but evolves following the Non-Critical Past (see below). $\nu(t) = K(t + c)^{-p}$ is the Modified Omori function (e.g., UTSU, 1961) and $Ke^{\alpha(Mj-Mc)}$ is the aftershock productivity. In this study, productivity is proportional to $10^{\alpha(Mj-Mc)}$ (HELMSTETTER et al., 2005; FELZER et al., 2004) for a cutoff magnitude $M_c = 1.0$ ($M_c = M_{cutoff}$).

The components of the parameter vector $\theta = (\mu, p, \alpha, c, K)$ of the ETAS model (Table 2) are obtained from the literature, except for the regional background seismicity rate μ which is fixed to δ_b^0 (and to δ_b^- inside the stress shadow) (GUO and OGATA, 1997; FELZER et al., 2004; HELMSTETTER et al., 2003, 2005). K is obtained from $K = n/(b \cdot \ln(10) \cdot (M_{max} - M_{min})/(p-1)/c^{(p-1)})$ (HELMSTETTER et al., 2005). The spatial distribution of aftershocks is assumed to be Gaussian,

Table 2

Parameters used in the synthetic catalogues

Parameter		Value
Magnitude-frequency	a value	4.4
	b value	1
	M_{min}	1
	M_{max}	6
Background	δ_b^0 (events/day/degree^2)	0.008
	δ_b^- (events/day/degree^2)	0.1 δ_b^0
ETAS clustering	p value	1.1
	α (magnitude^{-1})	1
	c (days)	0.001
	K	0.004

such that $\sim 99\%$ of aftershocks occur inside a circle of radius $L = 0.01 \times 10^{0.5M}$ from the main shock.

Aftershocks also obey Båth's law, in which the difference in magnitude between the main shock and its largest aftershock Δm is fixed to 1.0 to ensure that all aftershocks have a magnitude $M < M_{max}$ (SHCHERBAKOV et al., 2005). Note that the synthetic catalogs are more naturally defined using $\delta_{tot} = \delta_b^0 + \delta_{aft}$, where δ_{aft} represents ETAS clustering. In natural catalogs, this more accurately reflects the total seismicity, including natural aftershock sequences. Different δ_{tot} were tested by changing the cutoff magnitude M_{cutoff} of synthetic catalogues. Variation of $M_{min} = [1, 2, 3]$ (i.e., $\delta_{tot} \sim [4.95, 0.42, 0.038]$ events/degree^2/year), provides the capability to study theoretical precursory seismicity in different active seismic regions.

Figure 10 shows the synthetic seismicity, calculated as detailed above. On the left is shown a synthetic catalog based on the Non-Critical PAST, with a reverse fault ($L = 200$ km, $W = 10$ km, dip $= 45°$, expected magnitude $M \sim 7.3$) located in the center of an 18-degree square region. On the right is shown a similar synthetic seismicity catalog with no Non-Critical PAST signal, i.e., background

seismicity with random ETAS events, as formulated above, for use as a null hypothesis.

Figure 11 shows the normalized inverse TM metric for the synthetic seismicity catalogs shown in Fig. 10. Figure 11a is the inverse TM metric for the Non-Critical PAST catalog of Fig. 10a, while Fig. 11b shows the inverse TM metric for the random catalog of Fig. 10b. Note that both have significant breaks at year 15, related to a large event and its associated ETAS aftershock sequence.

The PI index calculations for an ergodic and a nonergodic time period for the catalog of Fig. 10a are shown in Fig. 12a and Fig. 12c, respectively. Figure 12e shows the PI index calculation for the same ergodic time period as Fig. 11a, but for the random null hypothesis catalog of Fig. 10b. Here the calculation is for events of $M \geq 1$ and a discretization boxsize of 1 degree. Figure 12a is calculated for a forecast time period of year 6 through year 14. Figure 12c is calculated for a forecast time period of year 6 through year 16. Figure 12e is calculated for year 6 through year 14 again, but for the catalog shown in Fig. 10b, as already noted. Red designates all values of the $\Delta P > 0$. Here we see that the forecast using the ergodic time period (Fig. 12a)
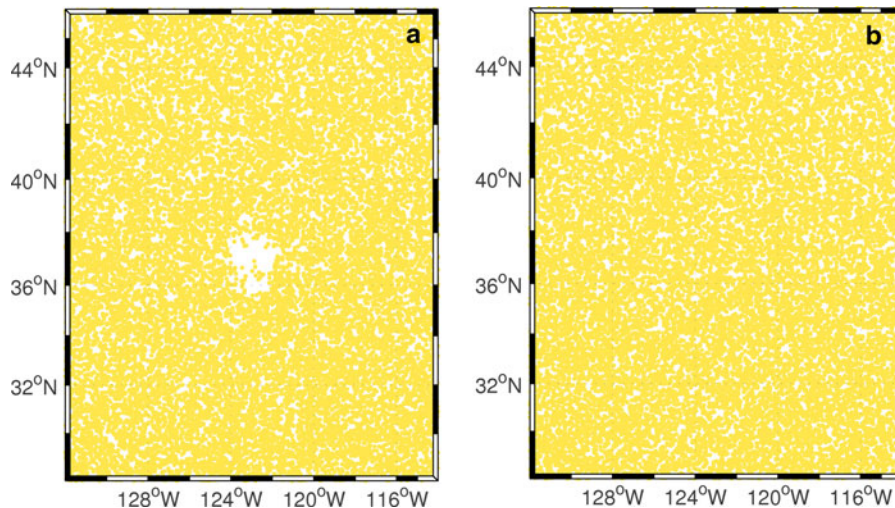

Figure 10
Synthetic seismicity plots. **a** Synthetic catalog based on the Non-Critical PAST. A reverse fault ($L = 200$ km, $W = 10$ km, dip $= 45°$, expected magnitude $M \sim 7.3$) is located in the center of an 18-degree square region. A stress *shadow* is created at $t = 0$ and decreases in size through time, until $t_f = 20$ years. The density of background events is $\delta_b^0 = 0.008$ event/day/degree (and $\delta_b^- = 0.1\delta_b^0$ inside the stress shadow) such that only events of magnitude $1 < M < 6$ occur in the 20 years time frame. Background events produce aftershocks which can also produce their own aftershocks following the ETAS model and Bath's law ($\Delta m = 1$). **b** A similar synthetic seismicity catalog with no Non-Critical PAST signal, i.e., background seismicity with random ETAS events
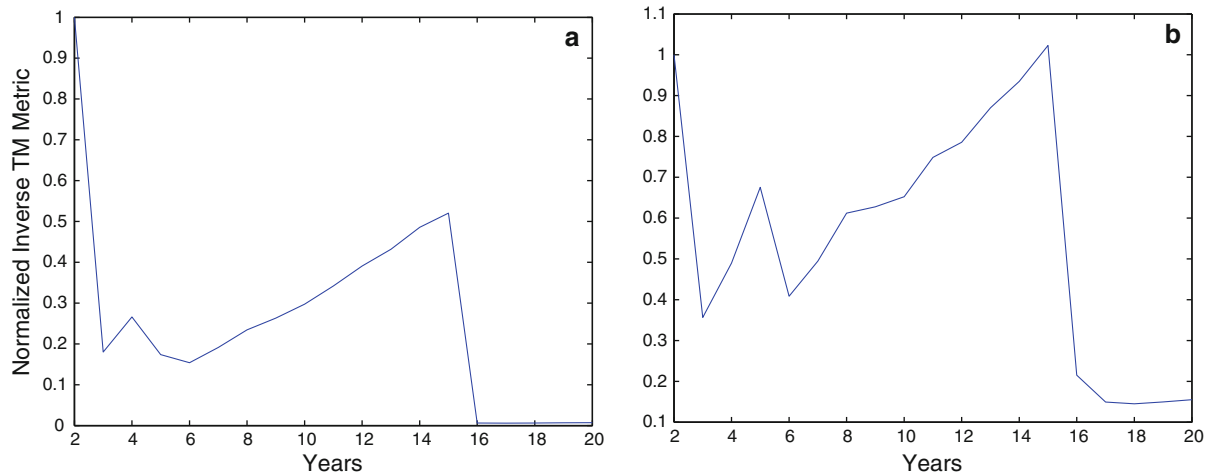
Figure 11
Plot of the inverse TM metric for the synthetic seismicity catalogs shown in Fig. 10. **a** The inverse TM metric, normalized to the first value, for the Non-Critical PAST catalog of Fig. 10a, while **b** shows the inverse TM metric for the random catalog of Fig. 10b

successfully forecasts the location of the upcoming event, while the random catalog for the same time period fails to forecast the event (Fig. 12e). More importantly, the forecast over the nonergodic time period (Fig. 12c) also fails to forecast the upcoming event. Note that we have not computed ROC diagrams for this test, as the catalog ends just prior to the occurrence of the large event at year 20 and such a test would not be relevant for this data set.

Figures 12b, 12d, and 12f show the seismicity rate change, $\Delta S'$, for the same catalogs and time periods as in Figs. 12a, 12c, and 12e. The color scale is normalized to the maximum value, where red is activation and blue is quiescence. Figure 12b confirms that the PI index is locating the anomalous quiescence associated with the stress shadow from the recurring large earthquake. For the nonergodic time period, Fig. 12d, the absolute value of that quiescence is significantly smaller, relative to the activation in the aftershock sequence from the large event in year 15. This results in the loss of significant power in the PI signal and a failure to forecast the upcoming event in Fig. 12b. This helps to explain the results for Taiwan in Section 3.1.2. Again, the identification of ergodic regions of phase space can significantly improve the forecast capability of the PI method in particular, and seismicity-based forecasting techniques in general.

4. Conclusions

In this work we employ the Thirumalai–Mountain fluctuation metric and data from existing seismic monitoring networks to identify the presence of punctuated ergodicity, an equilibrium property, in the dynamics of the natural earthquake fault system in three different tectonic regions; California, Taiwan, and eastern Canada. Because stationarity is a necessary but not sufficient condition for ergodicity, the identification of the appropriate spatial, temporal, and magnitude parameter ranges for ergodic behavior also ensures that the spatial and temporal averages are stationary and equivalent for those same regions of space and time.

After the identification of the ergodic regions for each catalog, we investigated the behavior of a forecasting technique that uses seismicity data and is linked intrinsically to the statistics of the seismic catalog, the PI index. The application of the PI index to both ergodic and nonergodic minimum magnitude cutoffs in eastern Canada provides evidence that ergodic periods provide significantly better forecasts, and that this is a result of the identification of stable, long-term seismicity rates which result in a reduction in the number of false positives.

We also tested the forecast capability of the PI index for ergodic and nonergodic time periods in Taiwan and synthetic catalogs. This analysis provides
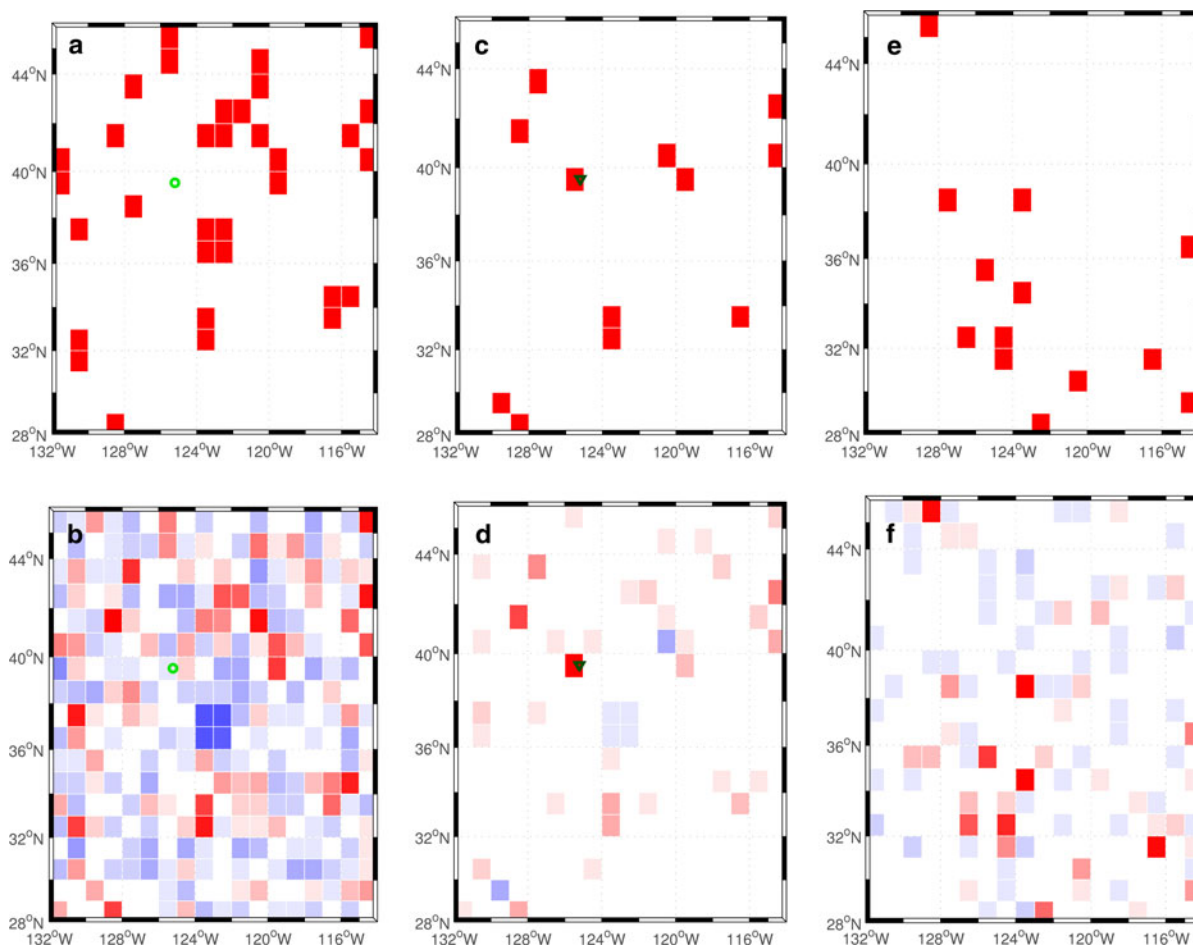
Figure 12
Plot of the PI index, ΔP, and seismicity rate change, ΔS, for $M \geq 1$ and a discretization boxsize of 1 degree, for the catalogs shown in Fig. 10.
a PI index for the Non-Critical PAST catalog of Fig. 10a and a forecast time period of Year 14–Year 6. *Red* designates all values of the $\Delta P > 0$; **b** ΔS for the catalog and time period shown in **a**. The *color scale* is linear, *blue* to *white* to *red*, where *blue* represents relative quiescence and *red* represents relative activation, normalized to the maximum value. **c** ΔP for the Non-Critical PAST catalog of Fig. 10a and a forecast time period of Year 16–Year 6; **d** ΔS for the catalog and time period shown in **c**; **e** PI index for the random catalog of Fig. 10b and a forecast time period of Year 14–Year 6; and **f** ΔS for the catalog and time period shown in **e**

evidence that the affect of larger events in the catalog and their associated aftershocks, which break ergodicity, leads to an overestimation of the background rate and an inability to locate some portion of future events. These misses appear to be linked to anomalous quiescence, which is more difficult to identify as a result of the high activation rate from aftershock occurrence. This affect, associated with aftershock sequence, may also be important for smaller amplitude foreshock sequences, and suggests that using the TM metric to identify ergodic periods will facilitate improvement of the efficacy of forecasting methodologies that focus on activation as well as quiescence.

Finally, comparison with methods that require declustering, also shown in Section 3.1.2, shows that the TM metric is both efficient and accurate in isolating regions of both ergodic and nonergodic behavior. Overall, our results lead to the conclusion that the TM metric provides a clear and useful method for identifying stationary regions of phase space associated with natural earthquake catalogs, and can be used to improve the forecasting capability of the PI index and other seismicity-based forecasting techniques that rely on stable, long-term averages. Future work will include the extension of testing to more realistic and varied synthetic catalogs, attempts

to identify methods for further improvement of both the PI index and other seismicity-based forecasting methods, and the development of a declustering algorithm based on the TM metric.

Acknowledgments

REFERENCES

ADAMS, J. E. and BASHAM, P. W. (1989), *The seismicity and seismotectonics of Canada east of the Cordillera,* Geoscience Canada 16, 3–16.

BOWMAN, D. D., OUILLON, G., SAMMIS, C. G., SORNETTE, A., and SORNETTE, D. (1998), *An observational test of the critical earthquake concept,* J. Geophys. Res. 103, 24,359–24,372.

BREHM, D. J. and BRAILE, L. W. (1998), *Intermediate-term earthquake prediction using precursory events in the New Madrid Seismic Zone,* Bull. Seismol. Soc. Am. 88, 564–580.

BUFE, C. G. and VARNES, D. J. (1993), *Predictive modeling of the seismic cycle of the greater San Francisco Bat region,* J. Geophys. Res. 98, 9871–9883.

DIETERICH, J. (1994), *A constitutive law for rate of earthquake production and its application to earthquake clustering,* J. Geophys. Res. 99, 2601–2618.

DIETERICH, J. H., CAYOL, V., and OKUBO, P. (2000), *The use of earthquake rate changes as a stress meter at Kilauea volcano,* Nature 408, 457–460.

DODGE, D. A., BEROZA, G. C., and ELLSWORTH, W. L. (1996), *Detailed observations of California foreshock sequences: Implications for the earthquake initiation process,* J. Geophys. Res. 101, 22371–22392.

EVISON, F. F. and RHOADES, D. A. (2004), *Demarkation and scaling of long-term seismogenesis,* Pure Appl. Geophys. 161, 21–45.

FELZER, K. R., ABERCROMBIE, R. E., and EKSTRÖM, G. (2004), *A common origin for aftershocks, foreshocks, and multiplets,* Bull. Seismol. Soc. Am. 94, 88–98.

FERGUSON, C. D., KLEIN, W., and RUNDLE, J. B. (1999), *Spinodals, scaling, and ergodicity in a threshold model with long-range stress transfer,* Phys. Rev. E 60,1359–1374.

GUO, Z. and OGATA, Y. (1997), *Statistical relations between the parameters of aftershocks in time, space, and magnitude,* J. Geophys. Res. 102, 2857–2873.

GUTENBERG, B. and RICHTER, C. F. (1944), *Frequency of earthquakes in California,* Bull. Seismol. Soc. Am. 34, 185–188.

HABERMANN, R. E. (1983), *Teleseismic detection in the Aleutian Island Arc,* J. Geophys. Res. 88, 5056–5064.

HABERMANN, R. E. (1987), *Man-made changes of seismicity rates,* Bull. Seism. Soc. Am. 77, 141–159.

HELMSTETTER, A., KAGAN, Y. Y., and JACKSON, D. D. (2005), *Importance of small earthquakes for stress transfers and earthquake triggering,* J. Geophys. Res. 110, doi:10.1029/2004JB003286.

HELMSTETTER, A., OUILLON, G., and SORNETTE, D. (2003), *Are aftershocks of large Californian earthquakes diffusing?* J. Geophys. Res. 108, doi: 10.1029/2003JB002503.

HOLLIDAY, J., CHEN, C., TIAMPO, K. F., RUNDLE, J. B., and TURCOTTE, D. L. (2007), *A RELM earthquake forecast based on pattern informatics,* Seis. Res. Lt. 78, 87–93.

HOLLIDAY, J. R., NANJO, K. Z., TIAMPO, K. F., RUNDLE, J. B., TIAMPO, K. F., and TURCOTTE, D. L. (2005), *Earthquake forecasting and its verification,* Nonlinear Processes in Geophys. 12, 965–977.

HOLLIDAY, J. R., RUNDLE, J. B., TIAMPO, K. F., KLEIN, W., and DONNELLAN, A. (2006a), *Systematic procedural and sensitivity analysis of the Pattern Informatics method for forecasting large (M > 5) earthquake events in southern California,* Pure Appl. Geophys., doi:10.1007/s00024-006-0131-1.

HOLLIDAY, J. R., RUNDLE, J. B., TIAMPO, K. F., and TURCOTTE, D. L. (2006b), *Using earthquake intensities to forecast earthquake occurrence times,* Nonlinear Processes in Geophysics 13, 585–593.

HOLMES, P., LUMLEY, J. L., and BERKOOZ, G., *Turbulence, Coherent Structures, Dynamical Systems and Symmetry* (Cambridge, University Press, U.K. 1996).

JIMÉNEZ, A., TIAMPO, K. F., LEVIN, S., and POSADAS, A. (2005), *Testing the persistence in earthquake catalogs: The Iberian Peninsula,* Europhys. Lett., doi:10.1209/epl/i2005-10383-8.

JOLLIFFE, I. T. and STEPHENSON, D. B., *Forecast Verification: A Practitioner's Guide in Atmospheric Science* (John Wiley, Hoboken, N. J. 2003).

KEILIS-BOROK, V. I. (1999), *What comes next in the dynamics of lithosphere and earthquake prediction?* Phys. Earth Planet. Int. 111, 179–185.

KLEIN, W., RUNDLE, J. B., and FERGUSON, C. D. (1997), *Scaling and nucleation in models of earthquake faults,* Phys. Rev. Lett. *78,* 3793–3796.

MARSAN, D. (2003), *Triggering of seismicity at short timescales following Californian earthquakes*, J. Geophys. Res. *108*, 2266, doi:10.1029/2002JB001946.

MATTHEWS, M.V. and REASENBERG, P. (1987), *Comment on Habermann's method for detecting seismicity rate changes,* J. Geophys. Res. *92*, 9443–9445.

MIGNAN, A. (2008a), *The Non-Critical Precursory Accelerating Seismicity Theory (NC PAST) and limits of the power-law fit methodology,* Tectonophysics *452,* doi: 10.1016/j.tecto.2008.02.010.

MIGNAN, A. (2008b), *The stress accumulation model: Accelerating moment release and seismic hazard,* Adv. Geophys. *49*, doi: 10.1016/S0065-2687(07)49002-1.

MIGNAN, A., KING, G. C. P., and BOWMAN, D. D. (2007), *A mathematical formulation of accelerating moment release based on the Stress Accumulation model,* J. Geophys. Res. *112*, B07308, doi: 10.1029/2006JB004671.

MIGNAN, A. and TIAMPO, K. F. (2010), *Testing the Pattern Informatics index on synthetic seismicity catalogues based on the Non-Critical PAST,* Tectonophysics *483*, 255–268, doi:10.1016/j.tecto.2009.10.023.

MOGI, K. (1969), *Some features of recent seismic activity in and near Japan (2), Activity before and after large earthquakes,* Bull. Earthquake Res. Inst., Univ. Tokyo *47*, 395–417.

MOGI, K. (1977), *Seismic activity and earthquake predictions,* Proc. Symp. on Earthquake Prediction, Seis. Soc. Japan, 203–214.

MOGI, K. (1979), *Two kind of seismic gaps,* Pure Appl. Geophys. *117,* 1172–1186.

MOORE, E. F. (1962), *Machine models of self reproduction*. In Proc. Fourteenth Symp. Appl. Math., 17–33.

MORI, H. and KURAMOTO, Y. *Dissipative Structures and Chaos* (Springer-Verlag, Berlin 1998).

MOUNTAIN, R. M. and THIRUMALAI, D. (1992), *Ergodicity and loss of dynamics in supercooled liquids,* Phys. Rev. A *45*, 3380–3383.

OGATA, Y. and ZHUANG, J. (2006), *Space-time ETAS models and an improved extension,* Tectonophysics *413*, 13–23.

OGATA, Y. (1992), *Detection of precursory seismic quiescence before major earthquakes through a statistical model*, J. Geophys. Res. *97*, 19845–19871.

OKADA, Y. (1992), *Internal deformation due to shear and tensile faults in a half-space,* Bull. Seismol. Soc. Am. *82*, 1018–1040.

ORIHARA, Y., NODA, Y., NAGAO, T., and UYEDA, S. (2002), *A possible case of SES selectivity at Kozushima island, Japan,* J. Geodyn. *33*, 425–432.

PAPAZACHOS, B. C., KARAKAISIS, G. F., PAPAZACHOS, C. B., and SCORDILIS, E. M. (2007), *Evaluation of the results for an intermediate-term prediction of the 8 January, 2006 $M_w = 6.9$ Cythera earthquake in the Southwestern Aegean,* Bull. Seismol. Soc. Am. *97*, 347–352, doi: 10.1785/0120060075.

REASENBERG, P. A. (1985). *Second-order moment of central California seismicity,* J. Geophys. Res. 90, 5479–5495.

RUNDLE, J. B., KLEIN, W., TIAMPO, K. F., and GROSS, S. (2000), *Linear pattern dynamics of nonlinear threshold systems,* Phys. Rev. E *61*, 2418–2432.

RUNDLE, J. B., TIAMPO, K. F., KLEIN, W., and SÁ MARTINS, J. S. (2002), *Self-organization in leaky threshold systems: The influence of near mean field dynamics and its implications for earthquakes, neurobiology and forecasting,* Proc. National Acad. Sci., U.S.A., Suppl. 1, *99*, 2463.

SAVAGE, J. C. (1983), *A dislocation model of strain accumulation and release at a subduction zone,* J. Geophys. Res. *88*, 4984–4996.

SHCHERBAKOV, R., TURCOTTE, D. L., and RUNDLE, J. B. (2005), *Aftershock statistics,* Pure Appl. Geophys. *162*, 1051–1076.

THIRUMALAI, D., MOUNTAIN, R. D., and KIRKPATRICK, T. R. (1989), *Ergodic behavior in supercooled liquids and in glasses,* Phys. Rev. A *39*, 3563–3574.

THIRUMALAI, D. and MOUNTAIN, R. D. (1993), *Activated dynamics, loss of ergodicity, and transport in supercooled liquids,* Phys. Rev. E *47,* 479–489.

TIAMPO, K. F., RUNDLE, J. B., KLEIN, W., HOLLIDAY, J., SÁ MARTINS, J. S., and FERGUSON, C. D. (2007), *Ergodicity in natural earthquake fault networks,* Phys. Rev. E *75*, 066107.

TIAMPO, K. F., RUNDLE, J. B., and KLEIN, W. (2006a), *Premonitory seismicity changes prior to the Parkfield and Coalinga earthquakes in southern California,* Tectonophysics *413*, 77–86.

TIAMPO, K. F., RUNDLE, J. B., and KLEIN, W. (2006b), *Stress shadows determined from a phase dynamical measure of historic seismicity,* Pure Appl. Geophys. doi:10.1007/200024-006-0134-y.

TIAMPO, K. F., RUNDLE, J. B., KLEIN, W., SÁ MARTINS, J. S., and FERGUSON, C. D. (2003), *Ergodic dynamics in a natural threshold system*, Phys. Rev. Lett. *91,* 238501.

TIAMPO, K. F., RUNDLE, J. B., McGINNIS, S., GROSS, S., and KLEIN, W. (2002), *Mean-field threshold systems and phase dynamics: An application to earthquake fault systems,* Europhys. Lett. *60*, 481–487.

TODA, S., STEIN, R. S., and SAGIYA, T. (2002), *Evidence from the AD 2000 Izu Islands earthquake swarm that stressing rate governs seismicity*, Nature *419*, 58–61.

TOYA, Y., TIAMPO, K.F., RUNDLE, J.B., CHEN, C., LI, H., and KLEIN, W. (2009), *Pattern Informatics approach to earthquake forecasting in 3-D*, Concurrency and Computation: Practice and Experience, doi: 10.1002/cpe.1531.

UTSU, T. (1961), *A statistical study on the occurrence of aftershocks,* Geophys. Mag. *30*, 521–605.

WIEMER, S. (2005), A software package to analyze seismicity: ZMAP. (http://www.earthquake.ethz.ch/software/zmap).

WIEMER, S. and WYSS, M. (2000), *Minimum magnitude of completeness in earthquake catalogs: Examples from Alaska, the Western United States, and Japan*, Bull. Seismol. Soc. Am. *90*, 859–869.

WYSS, M., and WIEMER, S. (1997), *Two current seismic quiescences within 40 km of Tokyo*, Geophys. J. Int. *128*, 459–473.

WU, Y.-M., CHANG, C.-H., ZHAO, L., TENG, T.-L., and NAKAMURA, M., (2008), *A comprehensive relocation of earthquakes in Taiwan from 1991 to 2005,* Bull Seismol. Soc. Am. *98*, 1471–1481.

ZÖLLER, G., HAINZL, S., and KURTHS, J. (2000), *Observation of growing correlation length as an indicator for critical point behavior prior to large earthquakes*, J. Geophys. Res. *106*, 2167–2175.